Discover Mechanical Engineering

RESEARCH Open Access

Influence of the shank geometry on the joint formation of the versatile self-piercing riveting of ultra-high-strength steel-aluminium and aluminium-aluminium assemblies

P. K. Kaimann[1*], N. Ritter[1], M. Bobbert[1] and G. Meschut[1]

*Correspondence:
P. K. Kaimann
pia.kaimann@lwf.uni-paderborn.de
[1]Paderborn University, Warburger Str. 100, 33098 Paderborn, Germany

Abstract

To reduce CO_2 emissions, the automotive industry is adopting multi-material structures. Fusion-based joining reaches its limits for aluminium–steel due to brittle intermetallic phases and mismatched thermophysical properties; therefore, mechanical joining (e.g., SPR) is used. Though conventional SPR requires tool changes for different stack-ups. Versatile self-piercing riveting (V-SPR) addresses this with an extended punch actuator and a multi-range-capable rivet (Kappe in PERD 16:363–378, 2022), enabling joints up to 600 MPa across varying thicknesses without retooling. With the use of ultra-high-strength steels up to 1000 MPa, optimisation is required. This study quantifies how rivet shank geometry affects joint formation using a design of experiments and validated 2D axisymmetric FE simulations. The optimum depends strongly on the material system. For CP1000–EN AW-6014, maximum interlock f is predicted for a medium shank thickness of about 0.73 mm, a small internal foot radius of 0.620 mm and a deeper drill depth of 3.136 mm, yielding f_{fc} = 0.4503 mm with a desirability of 0.954. For EN AW-6014–EN AW-6014, the optimum shifts to a thinner shank of 0.670 mm, a larger internal foot radius of 0.820 mm and a shallow drill depth of 2.30 mm, giving f_{fc} = 0.3023 mm with a desirability of 1.0. A compromise geometry of 0.713 mm shank thickness, 0.776 mm internal foot radius and 2.755 mm drill depth achieves f_{fc} = 0.3641 mm for CP1000–aluminium and f_{fc} = 0.1851 mm for aluminium–aluminium with an overall desirability D = 0.6378, expanding V-SPR to ultra-high-strength steel–aluminium joints while maintaining aluminium joinability.

1 Introduction

In the automotive industry, the reduction of carbon dioxide (CO_2) emissions has become a fundamental objective driven by increasingly stringent environmental regulations and the global push toward sustainable mobility [2]. One of the most effective approaches to meet these demands is the implementation of lightweight construction strategies [3]. In practice, these strategies increasingly rely on multi material body in white concepts

that combine aluminium and ultra high strength steels, and this material mix creates critical joining interfaces where UHSS elements such as rocker panels, B pillars and side ring reinforcements must be connected to aluminium floor assemblies, side panels, roof frames and cast or extruded nodes, which places high demands on the applied joining technology [4]. However, the implementation of such lightweight concepts frequently relies on the use of multi-material systems, which pose substantial challenges for conventional joining processes. In particular, thermal joining technologies, such as fusion-based processes that involve local melting and solidification, often reach their limits when applied to dissimilar materials, such as aluminium alloys and high-strength steels, due to the formation of brittle intermetallic phases and mismatches in thermophysical properties [5]. In contrast, mechanical joining technologies provide a viable and increasingly important alternative [6].

2 Self-piercing riveting

Self-piercing riveting (SPR) is particularly suited to joining multi-material combinations, such as steel and aluminium, without the need for a pre-hole. The joining principle is based on a combination of form and force closure, achieved in a single stroke with accessibility from both sides of the joint. Figure 1 shows the process sequence.

The riveting sequence begins with the positioning of the components between the punch and die. The blank holder applies a preload to prevent displacement of the components during the process. The rivet is then advanced toward the sheets and pressed into the punch side sheet by the punch. As the rivet has cut the punch side sheet, its shank reaches the die side sheet and is radially spread and compressed by the resistance of the die geometry. This expansion results in the formation of the interlock, which binds the sheets in a form-fit and force-fit connection. After the forming stage, the punch and the blank holder retract, and the joint remains completed [7]. This sequence enables a high degree of process reliability and repeatability, especially in automated production environments. However, due to the rigid tool system, the formation of a correct connection depends on the correct selection of the rivet die combination for the respective material geometry combination [8].

2.1 Tumbling self-piercing riveting

Tumbling self-piercing riveting is an innovative joining process that improves control of material flow and increases process versatility by superimposing an orbital tumbling motion onto the punch during riveting [9]. First, the components to be joined are positioned and securely fixed, and the rivet element is placed. The punch then initially

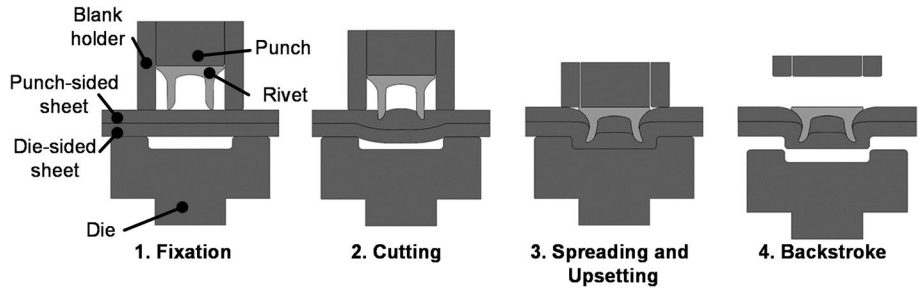

Fig. 1 Process sequence of the self-piercing riveting (SPR) [7]

penetrates the upper joining partners in a purely linear motion, comparable to the conventional self-piercing riveting process. At a defined penetration depth, the superimposed tumbling motion of the punch begins, altering the contact conditions between the punch, the rivet, and the material. As a result of the combined linear and tumbling movements, the rivet is formed, and the characteristic joint geometry is created. The process offers a high degree of flexibility, as it can be adapted to different material combinations without requiring tooling changes. In addition, the required process forces are reduced due to the optimised contact conditions, and the applicability of the process is extended to multi-material systems with differing mechanical properties. However, the available literature mainly addresses dual-phase steels such as HCT590X + Z with tensile strengths of around 600 MPa. For steels with tensile strengths of up to 1000 MPa, no direct application data are reported in the investigated studies, indicating that the process has not yet been established for these high-strength steel grades.

2.2 Low-frequency vibration-assisted riveting

Another innovative process is low-frequency vibration-assisted self-piercing riveting (LV-SPR), specifically developed for joining CFRP-aluminium composites [10]. The process addresses key limitations of conventional self-piercing riveting, particularly CFRP brittleness, which leads to material damage and insufficient interlock, thereby reducing joint load-bearing capacity. LV-SPR extends the conventional self-piercing riveting process by superimposing a controlled low-frequency oscillation in the punch feed direction using a servo-hydraulic system. This vibration concept enables stable, precise process control under high joining forces and represents an alternative to ultrasonic vibration assistance, which is generally constrained by system-level limitations in power transmission and load-bearing. During rivet penetration into the CFRP, periodic changes in friction direction reduce friction forces and significantly mitigate fibre breakage, delamination and interfacial debonding, while also lowering the required joining force. After CFRP penetration, vibration-induced material softening enhances radial expansion of the rivet shaft in aluminium, thereby increasing interlock. The combined effect of reduced CFRP damage and improved interlock results in enhanced mechanical performance, as evidenced by higher tensile-shear strengths compared to conventional self-piercing riveting [10].

2.3 Versatile self-piercing riveting

Versatile self-piercing riveting (V-SPR) is a novel approach to mechanical joining that addresses the limitations of rigid tool systems in multi-material constructions [1]. This process utilises a multi-range capable rivet and extended actuator technology to join different material thicknesses with a single rivet-die combination. Numerical investigations have demonstrated that rivet geometry, particularly shank geometry and length, has a significant influence on joint characteristics and material flow [11]. The versatile self-piercing riveting process proceeds in four stages, as shown in Fig. 2. On the left side of each step is a thin sheet combination, and on the right side is a thick sheet combination illustrated. In the first step, the sheets are fixed by the blank holder. In the second step, the inner punch drives the rivet through the punch-side sheet until it is cut. In the third step, the rivet expands into the die-side sheet, forming the interlock. After that, the outer punch deforms the rivet head protrusion onto the punch-side sheet, allowing the joint to

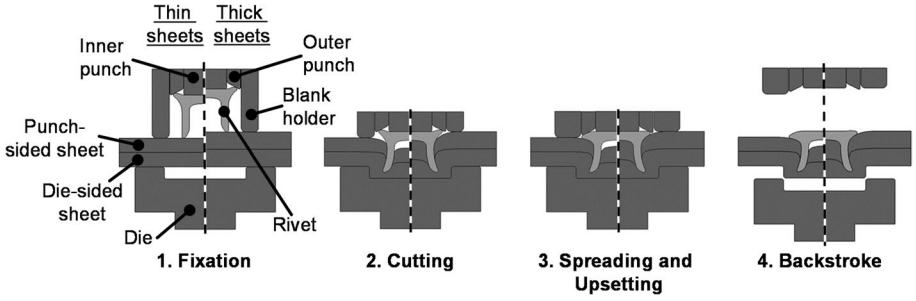

Fig. 2 Process sequence of the versatile self-piercing riveting (V-SPR) [1]

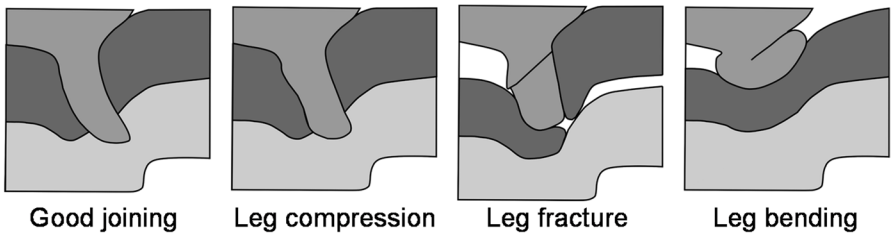

Fig. 3 Defects for joining of punch side ultra-high strength steel and die side aluminium sheets [13]

adapt to the actual sheet thickness and be additionally secured from the punch side. The fourth step is the backstroke of the two punches and the blank holder. This combined action of rivet expansion in the die-side material and head reshaping on the punch-side creates a force-fit and form-fit connection, ensuring a high load-bearing capacity and enabling flexible adaptation to varying material thickness combinations without the need to change rivets or dies [1].

Research in the field of V-SPR has so far focused primarily on the use of aluminium materials and mixed-material joints with steels up to a strength of 600 MPa in combination with aluminium [12]. However, in order to further qualify the technology for future lightweight construction requirements, the range of applications must be specifically expanded to include the use of ultra-high-strength materials with strengths of up to 1000 MPa.

2.4 Joining high-strength sheets with SPR

Joining ultra-high-strength steels with aluminium presents significant challenges for self-piercing riveting (SPR). The elevated strength of ultra-high-strength sheet metal on the punch side often leads to various rivet failure modes, including upsetting, fracture, or bending of the rivet shank, see Fig. 3 [13].

A direct increase in rivet hardness is not a feasible solution for preventing these rivet failures, as it compromises the ductility essential for the rivet expansion during the spreading process. This limitation is supported by the investigations of Yu et al., who analysed the influence of process parameters on the joint strength and failure behaviour of self-piercing riveted steel/aluminium hybrid joints. Their results show that joint strength increases only up to a certain rivet strength, depends non-linearly on the thickness ratio, and that, with a sheet thickness > 1.47 mm, the joint direction Al-Steel is

advantageous. The sheet material, thicknesses, and joint direction are decisive for the failure mode, not the rivet strength [14].

One possible approach is to generate a graded hardness profile by locally heat-treating the rivet [15]. This results in different strength levels within the rivet, for example, a hard rivet shank and a softer rivet head. So far, this method has been investigated only for punch-side sheets made from steel with a tensile strength of 600 MPa. However, the process also shows potential for application in ultra-high-strength steels. Another possible approach is to modify the die geometry to prevent plastic deformation of the rivet during its penetration into the ultra-high-strength punch-side sheet. The applied punch force must remain below the product of the rivet material's yield strength and its cross-sectional area. Enhancing the size of the die hollow and increasing the depth of the central elevation in mandrel dies reduces the requisite punch force [13].

Another option for improving the joinability of ultra-high-strength materials is the use of heat treatments. Local preheating of the joining zone, for example, by laser heating, can induce a local softening effect, thereby locally reducing the material strength and consequently decreasing the load acting on the rivet shank during the punching phase [16]. In contrast, thermally assisted self-piercing riveting (TA-SPR) employs inductive preheating of the ultra-high-strength steel sheets prior to conventional SPR. This technique uses an induction coil to locally increase the temperature of the punch-side sheet metal, improving formability and facilitating rivet penetration [17].

The review study [5] describes various specialised self-piercing riveting processes relevant to joining ultra-high-strength steels. These include the tumbling self-piercing riveting process described above and the pre-holed self-piercing riveting process explained below.

The pre-holed self-piercing riveting (PH-SPR) is a suitable process alternative for increasing the joinability of high-strength to ultra-high-strength materials, as the rivet load is reduced during the penetration phase. For CFRP in titanium sheets, improved form fit and higher joint strength were demonstrated compared to conventional SPR. The form-fit length and rivet head height are decisive factors, influenced by the metal sheet's formability and the joining force [18]. For DP590 and Al alloys, PH-SPR also reduces riveting force and energy requirements while improving performance, with a 4.8% increase in peak force and a 3.18-fold increase in energy absorption. The forming quality is primarily governed by rivet parameters such as lower rivet strength and greater rivet length [19].

Furthermore, there are special rivet geometries, such as the HDZ rivet, which meet the requirements for joining ultra-high-strength steels with tensile strengths of up to 1500 MPa [20]. However, these are designed for specific material combinations, which means that the rivet die combination must be adapted for new material combinations. For this reason, this study develops a versatile rivet geometry that can join both mixed-material connections made of ultra-high-strength steel and aluminium, as well as pure aluminium connections.

3 Experimental details

3.1 Materials

The rivet is composed of C35 B + Cr material. The sheets consist of EN AW-6014 temper T4 and ultra-high-strength steel CP 1000, which has a nominal strength of 980 to

1140 MPa. The chemical composition properties of the rivet material and the investigated materials, EN AW-6014 temper T4 and CP 1000, are presented in Table 1.

3.2 Experimental set-up

To validate the quality of the results, the simulation studies were compared with samples produced experimentally. The material combination CP 1000, with a 1.5 mm sheet thickness in EN AW-6014 T4 and a 2.0 mm sheet thickness, was joined using the rivet HDZ 5.5 × 5 H4 and die FM 0902218. The samples were created by joining square sheet metal blanks measuring 45 mm × 45 mm using the TUCKER® TRT080 joining system.

4 Numerical simulation

For the numerical investigation of the influence of shank geometry on joint formation, 2D axisymmetric simulation models, as shown in Fig. 4, were employed. This modelling approach builds on the preliminary investigations reported by Kappe et al. [24].

The finite element models were created with LS-DYNA and solved using an implicit scheme. The punches and the die were represented as elastic bodies to enable a detailed assessment of the forces acting during the process, and the punch motion was prescribed by constraining its nodes. The joining force of the die was evaluated in its lower region. Since no forces are measured within the blank holder, it can be treated as a rigid body to reduce the calculation time, while exerting a constant force throughout the experiment. Material behaviour in the simulation was defined using experimentally determined flow curves for CP 1000, EN AW-6014, and the rivet material in strength class H4. Cutting of the punch-side sheet was implemented through a geometric cutting criterion that was activated by the prevailing process conditions. From a sheet thickness of 0.8 mm on the punch side, the elements are deleted in the numerical simulation. The factor was determined experimentally by step setting tests, see Fig. 5.

The contact behaviour between the rivet and the EN AW-6014 sheet was modelled using the static coefficient of friction of 0.2 [25]. The contact behaviour between the rivet and the CP 1000 sheet, as well as the sheets themselves, was modelled using the static coefficient of friction of 0.12 [26].

The 2D simulation models are validated by comparing the micrograph, the force-displacement diagram, and the quality parameter of the joint formation of the HDZ rivet with hardness H4 for CP 1000 in EN AW-6014 with the simulation model of SPR, as shown in Fig. 6. The comparison reveals a very close correspondence between the simulated results and the experimental micrograph. In particular, the simulation captures the flow behaviour of the rivet material with high fidelity. The V-SPR model has been validated for EN AW-6014 in EN AW-6014 in previous studies [27].

In the following, the V-SPR simulation model is used to adjust the rivet shank geometry for the use of the multi-range-capable rivet by Kappe [12], in the following rivet K, in the material combination CP 1000 in EN AW-6014, as well as EN AW-6014 in EN AW-6014.

Table 1 Chemical composition properties of the rivet material C35 B + Cr [21]and the investigated materials EN AW-6014 temper T4 [22] and CP 1000 [23]

Chemical composition C35 B + Cr (weight%)										
Elements	Si	C	Cu	Mn	P	S	Cr		Mo	B
Min.		0.35		0.60						0.0008
Max.	0.3	0.40	0.25	0.90	0.025	0.025	0.3		-	0.005
Chemical composition EN AW-6014, T4 (weight%)										
Elements	Si	Fe	Cu	Mn	Mg	Cr	Zn		Ti	V
Min.	0.30			0.05	0.40					
Max.	0.60	0.35	0.25	0.20	0.80	0.20	0.10		0.10	0.10
Chemical composition CP 1000 (weight%)										
Elements	C	Si	Mn	P	S	Al	Cr + Mo	Ti + Nb	B	Cu
Max.	0.23	1.00	2.70	0.05	0.01	0.015-1.0	1.0	0.15	0.005	0.2

5 Design of experiment (DoE)

A statistical design of experiments method was employed to organise the sensitivity analyses effectively and optimise the rivet shank geometry. First, a sensitivity analysis is used to determine the individual effects of the rivet shank geometry parameters on the joint formation for the respective material combination. Optimisation is then used to derive rivet shank geometries that maximise the interlock for the individual material combinations, ultra-high-strength steel in aluminium and pure aluminium joints, as well as a rivet geometry that meets the requirements of both joining tasks. Using Minitab statistical software, a central composite design (CCD) was developed for the study. This CCD combines a two-factor factorial design with area-centred star points and includes at least one centre point [28].

5.1 Rivet parameters

The geometry of the rivet shank is particularly important for ensuring the successful cutting of the punch side sheet when using ultra-high-strength materials. The rivet shank must not deform or collapse during the punching process. Therefore, this study adapts the rivet shank of the multi-range capable rivet (K-rivet), shown in Fig. 7a, which was previously designed for materials with a strength of 600 MPa on the punch side in combination with aluminium and pure aluminium alloys [8]. Figure 7c shows the numerically determined failure behaviour of the K-rivet for the material combination CP 1000 in 1.5 mm sheet thickness in EN AW-6014 in 2.0 mm sheet thickness. The parameters of the factors are based on the geometric parameters of the HDZ rivet, as shown in Fig. 7b, at the upper limit and those of the K rivet at the lower limit. The aim is for the new rivet shank geometry to join both material combinations with CP 1000 on the punch side in aluminium and pure aluminium alloys.

In this study, the three geometric factors, shank thickness (d), drill depth (T), and internal foot radius (r_f), were selected to investigate their influence on joint formation numerically. For the numerical investigations, the V-SPR model was used. The validation presented above. Each geometry factor was tested at three levels (see Table 2). A design-of-experiments (DoE) screening study was run to determine the factor effects. In order to minimise the number of tests required for the numerical simulations, a partial factorial test plan was chosen. The quality-relevant parameter interlock (f) was used as the response variable. The minimum die-side material thickness (t_r) exceeded the critical value of 0.15 mm for the entire test plan and was therefore not included in the sensitivity analysis and optimisation.

The complete central composite design of the three factors is shown in Table 3.

6 Results and discussion

6.1 Sensitivity analysis of rivet geometry parameters

The sensitivity analysis is conducted in two stages. First, the effects of the rivet parameters are analysed for two material combinations: CP 1000 with a sheet thickness of 1.5 mm in EN AW-6014 with a sheet thickness of 2.0 mm, and EN AW-6014 with a sheet thickness of 1.5 mm in EN AW-6014 with a sheet thickness of 2.0 mm. The optimal riveting parameters were identified for each case by maximising the target variable, interlock. Subsequently, the optimal parameters for riveting were established for the two material combinations. Figures 8 and 9 show the main effects diagrams. Each curve

FE-simulation – Relevant parameters	
Simulation software	LS-Dyna
Solver	smp_d_R910
Analysis	Implicit
Section	Shell
Element formulation	15 – Axissymmertric solid
Material seperation criterion	Geometrical
Process control	Displacement (Punches)
Punch feed direction	Y-Axis

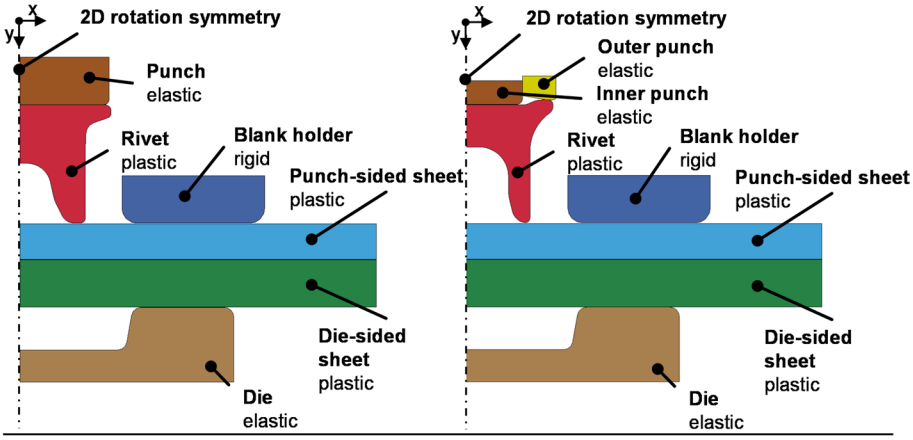

Fig. 4 Numerical setup of the SPR and the V-SPR joining process

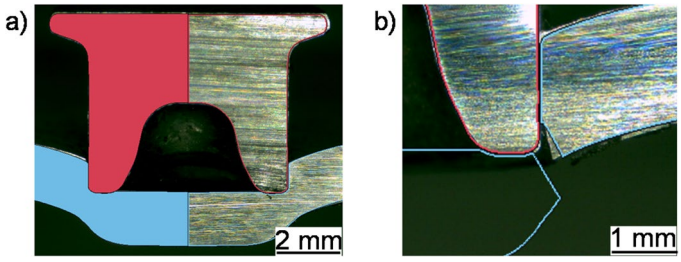

Fig. 5 Step setting tests and simulation in comparison **a** immediately before cutting and **b** in detail after cutting

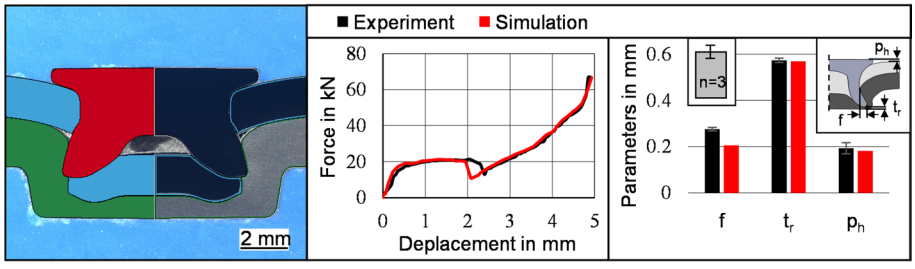

Fig. 6 Validation of the simulation model by comparing the micrograph, the force-displacement diagram, and the quality parameter (interlock f, minimum die side material thickness t_r and rivet head position p_h)

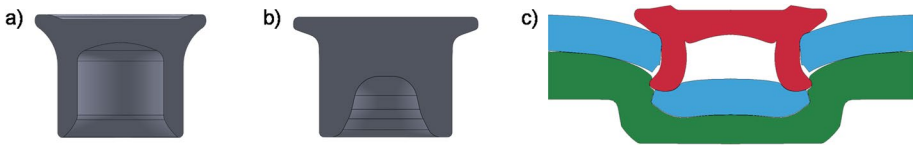

Fig. 7 **a** Rivet geometry of the multi-range capable rivet (K-rivet), **b** Rivet geometry of the HDZ rivet, **c** Numerically determined failure behaviour of the K-rivet for the material combination CP1000 in 1.5 mm sheet thickness in EN AW-6014 in 2.0 mm sheet thickness

Table 2 Varied rivet shank factors

Rivet factors	Acronym	Range in mm		
Shank thickness	d	0.67	0.735	0.80
Drill depth	T	2.30	3.20	4.10
Internal foot radius	r_f	0.62	0.72	0.82

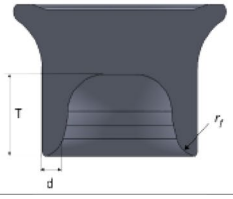

Table 3 Central composite design of the three factors

1	Shank thickness in mm	Drill depth in mm	Internal foot radius in mm
	0.67	**2.3**	**0.62**
2	0.8	2.3	0.62
3	0.67	2.3	0.82
4	0.8	2.3	0.82
5	0.67	4.1	0.62
6	0.8	4.1	0.62
7	0.67	4.1	0.82
8	0.8	4.1	0.82
9	0.67	3.2	0.72
10	0.8	3.2	0.72
11	0.735	3.2	0.62
12	0.735	3.2	0.82
13	0.735	2.3	0.72
14	0.735	4.1	0.72
15	0.735	3.2	0.72

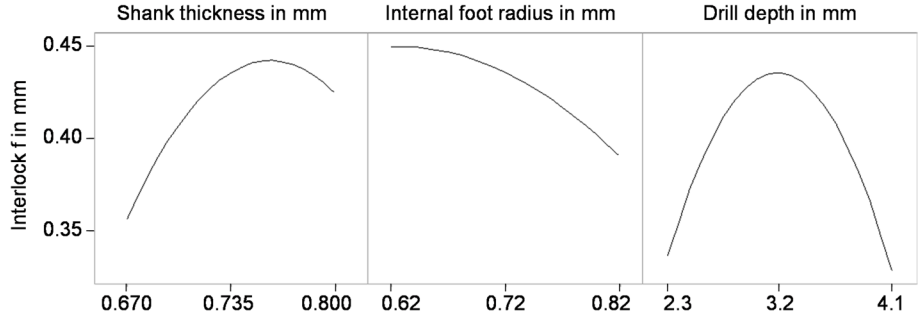

Fig. 8 Main effect diagram of the material combination CP 1000 in 1.5 mm in EN AW-6014 in 2.0 mm related to the three rivet parameters investigated: shank thickness (d), drill depth (T), and internal foot radius (r_f)

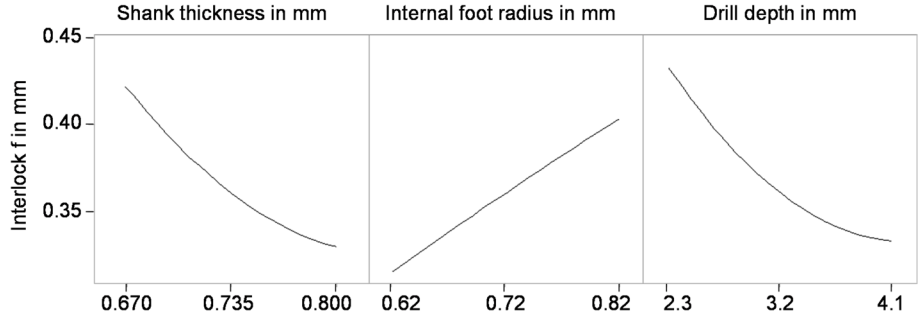

Fig. 9 Main effect diagram of the material combination EN AW-6014 in 1.5 mm in EN AW-6014 in 2.0 mm related to the three rivet parameters investigated: shank thickness (d), drill depth (T), and internal foot radius (r_f)

represents the mean predicted response at a given factor level, averaged over the levels of the remaining factors.

The main effect diagram of the material combination CP 1000 in EN AW-6014 for the interlock (Fig. 8) displays three clear trends. Firstly, the shank thickness shows a pronounced non-linear relationship: the interlock initially increases, reaches a maximum around 0.75 mm, and then decreases at higher thicknesses. Both minimal and substantial shank thicknesses are therefore unfavourable. This is because, with a smaller shank thickness, the rivet shank is compressed during joining ultra-high-strength steel, whereas with larger shank thicknesses, the rivet is prevented from expanding. Secondly, the effect of the internal foot radius is nearly monotonically adverse across the investigated range. A larger radius consistently reduces the interlock, while a smaller radius tends to increase it. This is because a smaller foot radius prevents premature rivet compression during punching. Thirdly, the drill depth, similar to the shank thickness, follows a curved trend with a maximum around 3.1 mm to 3.3 mm; both shallow depths (around 2.4 mm) and deeper depths (up to 4.0 mm) result in significantly lower interlock. This is due to the fact that a shallow depth prevents the rivet shank from spreading. At greater depths, the shank is compressed more due to its lower rigidity. A ranking of the influence strength can be inferred from the vertical span of the subplots: drill depth (the most substantial effect) ≥ shank thickness > internal foot radius (the most minor but consistently negative effect).

The main effect diagram of the material combination EN AW-6014 in EN AW-6014 for interlock is shown in Fig. 9. The shank thickness has an adverse effect within the examined range of approximately 0.70 mm to 0.80 mm; the mean interlock decreases nearly linearly from about 0.17 mm to 0.18 mm to approximately 0.08 mm. Therefore, a smaller shank thickness favours a higher interlock value. This is because, when joining aluminium combinations, significantly lower rivet stiffness is required during punching, resulting in a lower shaft thickness in the area under investigation, which significantly increases the spreading behaviour. Secondly, the internal foot radius has a positive main effect. As the radius increases (roughly 0.60 mm to 0.80 mm), the interlock increases almost uniformly from around 0.06 mm to approximately 0.16 mm. A larger foot radius is advantageous for use in aluminium, in contrast to use in CP 1000. The larger radius results in a more tapered rivet foot geometry, which improves cutting performance in aluminium. This allows the shaft to be filled earlier and gives the rivet increased spreading behaviour. Thirdly, the drill depth has an adverse effect, which is most noticeable at shallow depths: between about 2.4 mm and 3.2 mm, the interlock drops sharply from

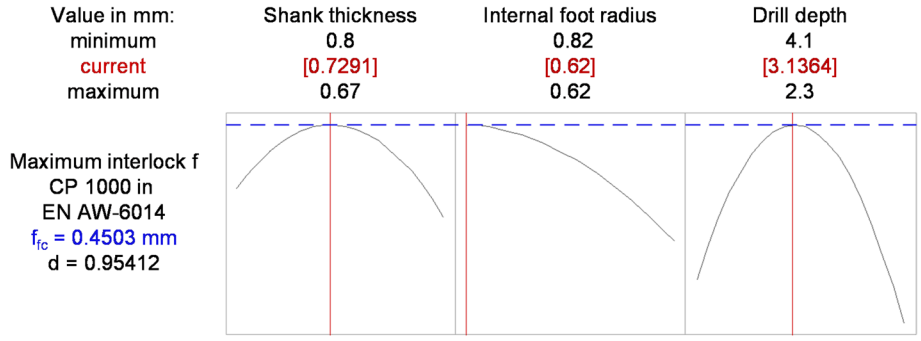

Fig. 10 Optimisation diagram of the rivet shank geometry for the material combination CP 1000 in 1.5 mm in EN AW-6014 in 2.0 mm related to the three rivet parameters investigated: shank thickness (d), drill depth (T), and internal foot radius (r_f)

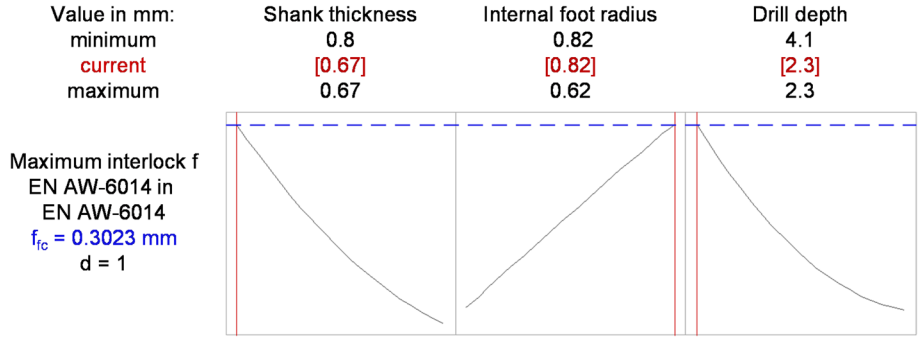

Fig. 11 Optimisation diagram of the rivet shank geometry for the material combination EN AW-6014 in 1.5 mm in EN AW-6014 in 2.0 mm related to the three rivet parameters investigated: shank thickness (d), drill depth (T), and internal foot radius (r_f)

roughly 0.18 mm, and the rate of decline then levels off at around 4.0 mm (final values near 0.08 mm). Due to the large drilling depth, the cavity for accommodating the slug is large, which means that the rivet is not stimulated to expand by the counterpressure of the retained slug. The vertical span of the subplots indicates similar levels of influence. The most significant changes are observed in the internal foot radius and drill depth, with shank thickness following closely.

6.2 Optimisation of rivet geometry parameters

The optimisation diagrams for the material combination CP 1000 in EN AW-6014 (Fig. 10) and the material combination EN AW-6014 in EN AW-6014 (Fig. 11) confirm these findings. To improve readability, the desirability value d shown in Figs. 10, 11 and 12 is briefly explained here. The desirability function maps the predicted response (interlock f) onto a dimensionless scale from 0 to 1, where $d = 0$ indicates an unacceptable outcome (below the specified lower bound) and $d = 1$ indicates full fulfilment of the optimisation target (i.e., the target region defined for maximising interlock is reached). Intermediate values $0 < d < 1$ represent partial target achievement according to the selected desirability function. In the single-response optimisations (Figs. 10 and 11), d directly corresponds to the target achievement for interlock (e.g., $d = 0.954$ for CP1000 in EN AW-6014 and $d = 1.000$ for EN AW-6014 in EN AW-6014) together with the predicted interlock ffc. For the combined optimisation across both material combinations,

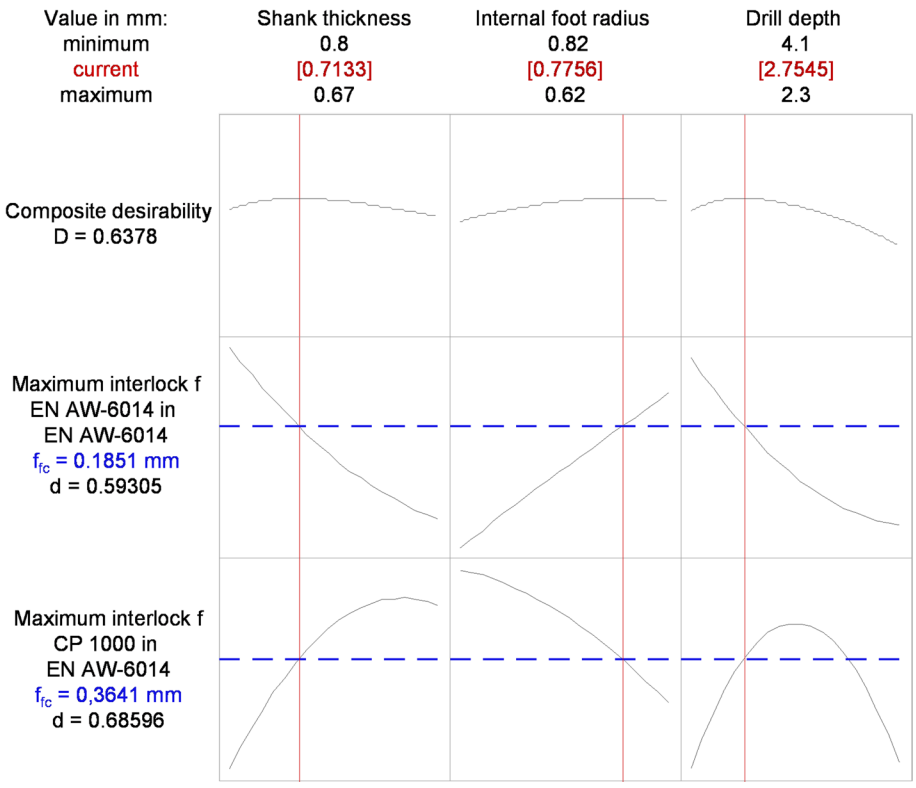

Fig. 12 Optimisation diagram of the rivet shank geometry for both material combinations (EN AW-6014 in 1.5 mm in EN AW-6014 in 2.0 mm and CP 1000 in 1.5 mm in EN AW-6014 in 2.0 mm) related to the three rivet parameters investigated: shank thickness (d), drill depth (T), and internal foot radius (r_f)

the overall desirability D aggregates the individual desirabilities and therefore quantifies the compromise quality (Fig. 12).

For CP 1000, a high composite degree of target achievement (d = 0.954) is achieved with a forecast interlock of f_{fc} = 0.4503 mm. The optimal rivet shank variables are a shank thickness of 0.7291 mm, the smallest possible internal foot radius of 0.620 mm, and a drill depth of 3.1364 mm.

For EN AW-6014 in EN AW-6014, the optimisation results for the rivet shank geometry in a marginal optimum with d = 1.000 and f_{fc} = 0.3023 mm are a shank thickness of 0.670 mm (minimum), an internal foot radius of 0.820 mm (maximum), and a drill depth of 2.30 mm (minimum). The material contrast between the effect directions, with a small internal foot radius for steel versus a large internal foot radius for aluminium, and medium versus minimum drill depth, thus becomes quantitatively tangible.

The combined optimisation of the rivet shank for both material combinations, shown in Fig. 12, results in a compromise with reduced overall desirability (D = 0.6378).

The standard setting found is: shank thickness 0.713 mm, internal foot radius 0.776 mm, and drill depth 2.755 mm. Under these conditions, the results are f_{fc} = 0.1851 mm (d = 0.593) for aluminium and f_{fc} = 0.3641 mm (d = 0.686) for CP 1000. Compared to the individual solutions, the drill depth is significantly reduced in favour of aluminium, the internal foot radius is shifted towards larger values, also in favour of aluminium, while the shank thickness lies between the respective material optima, thus limiting the loss for CP 1000. The compromise is therefore physically plausible, as it balances the opposing effects of internal foot radius and drill depth, and positions the shank

thickness in a range where the CP 1000 still operates close to its parabolic maximum without failing to meet the aluminium requirements.

Figure 13: *Numerical simulation results of the joint formation of the various optimums of the rivet shank geometry, on the right CP1000 in EN AW-6014, on the left EN AW-6014 in EN AW-6014, (a) Optimal rivet shank geometry for use in CP 1000 on the punch side, (b) Optimal rivet shank geometry for use in EN AW-6014 on the punch side, (c) Optimal rivet shank geometry for use in CP1000 and EN AW-6014 on the punch side and the diagram of resulting interlock.*

On the right-hand side, the material combination CP 1000 in EN AW-6014 is shown, and on the left-hand side, the combination EN AW-6014 in EN AW-6014. The figures illustrate (a) the rivet shank geometry optimised for use with CP 1000 on the punch side, (b) the geometry optimised for use with EN AW-6014 on the punching side, and (c) the compromise-based rivet shank geometry for combined use in CP 1000 and EN AW-6014. In addition, the diagram of the resulting interlock is shown, which quantitatively illustrates the respective quality of the connection.

The rivet geometry optimisation (a) shows that, for the combination CP 1000 in EN AW-6014, a small internal foot radius in conjunction with a medium drill depth of approximately 3.1 to 3.2 mm and a shank thickness of approximately 0.73 mm proves to be optimal. This parameter configuration enables good interlock formation. However, if this geometry is used for EN AW-6014 in EN AW-6014 connections, the connection quality deteriorates significantly. In particular, the small internal foot radius and the higher shank thickness hinder the material flow in the more ductile aluminium and thus reduce the achievable interlock.

The rivet geometry optimisation (b) shows that, in the pure aluminium material combination, a larger internal foot radius (≈approximately 0.82 mm), a low shaft thickness (≈approximately 0.67 mm), and a minimum drill depth (≈approximately 2.3 mm) have been identified as optimal. However, when these parameters are applied to the steel-aluminium combination with CP 1000, the geometry leads to unsatisfactory results. The

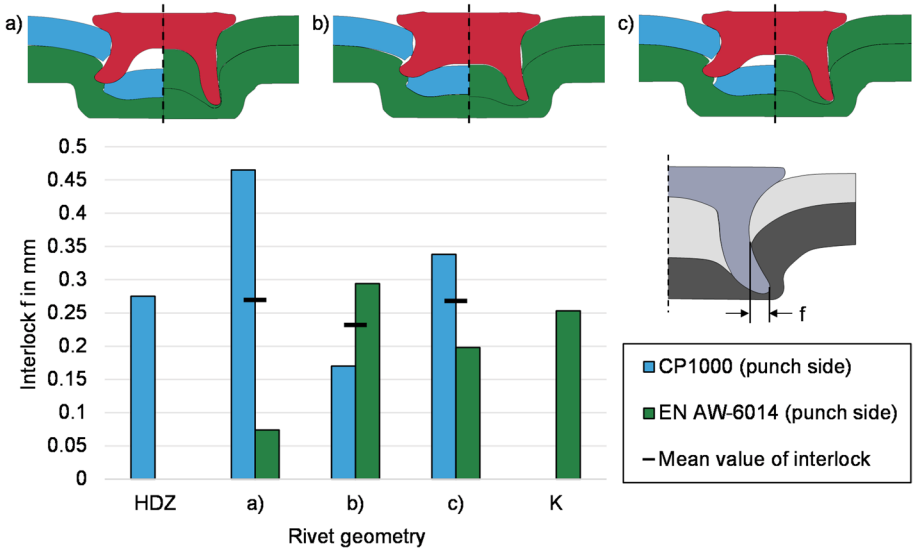

Fig. 13 shows the results of numerical simulations of joint formation with different optimisations of the rivet shank geometry

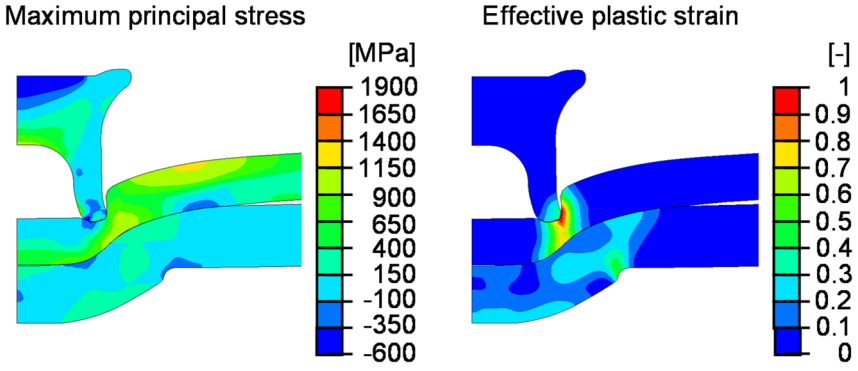

Fig. 14 Maximum principal stress and effective plastic strain of the rivet geometry (c) during the setting process of the material combination CP1000 in aluminium

i.O. ✓		EN AW-6014 (punch side)			CP 1000
n.i.O. ✗		1.0 mm	1.5 mm	2.0 mm	1.5 mm
EN AW-6014 (die side)	1.0 mm	✗	✗	✗	✓
	1.5 mm	✓	✓	✗	✓
	2.0 mm	✓	✓	✗	✓

Fig. 15 Numerical simulation results of additional material thickness combinations associated with the compromise-based rivet shank geometry (c). Assessment of connectability depending on the material configuration and sheet thickness

low shaft thickness promotes upsetting of the rivet shank, which, in combination with the low drill depth, results in a drastic reduction in interlock.

The compromise-based rivet shank geometry (c) (shank thickness ≈ 0.71 mm, internal foot radius ≈ 0.78 mm, drill depth ≈ 2.76 mm) represents a balanced solution that is functional in both material systems. Although it does not achieve the maximum possible interlock values of the specific optimisation in CP 1000, it does avoid significant failure mechanisms. In aluminium connections, on the other hand, stable, albeit slightly reduced, interlock values are achieved. This optimum thus offers the highest flexibility, as it covers both material combinations with satisfactory joining quality without requiring material-specific geometries to be adapted. Figure 14 shows the maximum principal stress and effective plastic strain during the setting process of the material combination CP1000 in aluminium. It can be seen that the rivet undergoes a slight deformation of 0.2 during penetration into the CP1000, but this does not lead to failure.

The suitability of the compromise-based rivet geometry (c) was numerically investigated for other material combinations. The corresponding results are shown in Fig. 15. For this purpose, additional material thickness combinations were added to the simulation using the identified optimal rivet geometry. The evaluation demonstrates that the developed rivet can join a broad range of aluminium-aluminium and steel-aluminium

combinations in a process-stable manner. In particular, stable joint formations with sufficient interlock are achieved for configurations with CP 1000 on the punch side and EN AW-6014 on the die side.

However, a clear limitation arises for configurations with aluminium positioned on the punch side at a sheet thickness of 2.0 mm. In these cases, no functional joint can be formed. The reason is the insufficient shank cavity volume of the rivet relative to the displaced material volume. The slug generated during penetration cannot be adequately accommodated, preventing sufficient radial expansion of the rivet shank and, consequently, the formation of a proper interlock. These results indicate that, although the developed geometry offers a high degree of versatility, it reaches its volumetric limits when joining thicker aluminium sheets on the punch side. Further adaptation of the shank cavity volume or drill depth would be required to reliably enable these configurations.

7 Conclusion

This study has demonstrated that the geometry of the rivet shank has a significant impact on the joint formation in the versatile self-piercing riveting (V-SPR). In particular, the parameters of shank thickness, drill depth, and internal foot radius have proven to be decisive factors for interlock formation and thus for the quality of the joint. While a medium shaft thickness, medium drill depth, and small internal foot radius produce the best results for the material combination of CP 1000 and EN AW-6014, a low shaft thickness, larger foot radius, and lower drill depth prove to be optimal for pure aluminium joints. These differences illustrate the contrasting requirements that ultra-high-strength steel in aluminium joints and pure aluminium joints place on rivet geometry.

However, the investigation enabled the development of a compromise-based rivet shank geometry that ensures a stable and reliable joining of both material systems despite reduced interlocks. This has enabled the extension of the application possibilities of the V-SPR process to ultra-high-strength materials, up to 1000 MPa, while maintaining the joining quality in aluminium combinations. The results thus prove that the targeted adaptation of the rivet shank geometry is an effective means of overcoming the limitations of previous joining technologies and significantly increasing the flexibility of V-SPR with regard to different material combinations.

There are various starting points for future research. First, the geometries determined in the numerical investigations should be verified by comprehensive experimental studies to ensure their practical suitability under real production conditions. In addition, it is necessary to determine the load-bearing capacity of the developed joints. Furthermore, the applicability of the developed rivet geometry for use with different sheet-thickness combinations should be systematically investigated.

Overall, it has been shown that optimising the rivet shank geometry makes a significant contribution to increasing the versatility of the versatile self-piercing riveting.

Acknowledgements

Funded by the Deutsche Forschungsgemeinschaft (DFG, German Research Foundation) – TRR 285/2 – Project-ID 418701707. The authors thank the German Research Foundation for their organisational and financial support.

Author contributions

P.K.: Conceptualisation, Methodology, Validation, Visualisation, Investigation, Formal analysis, Writing – original draft, Writing – review & editing. N.R.: Investigation, Formal analysis, Validation, Data curation. M.B.: Supervision, Writing – review & editing. G.M.: Resources, Funding acquisition, Supervision. All authors have read and agreed to the published version of the manuscript.

Funding
Open Access funding enabled and organized by Projekt DEAL. Funded by the Deutsche Forschungsgemeinschaft (DFG, German Research Foundation) – TRR 285/DFG, German Research Foundation. The authors thank the German Research Foundation for their organisational and financial support.

Data availability
The datasets used and/or analysed during the current study are available from the corresponding author on reasonable request.

Declarations

Ethical approval and Consent to participate
Not applicable. This study did not involve human participants, human data, or live vertebrate animals. All investigations were based on numerical simulations and experimental joining tests on metallic materials.

Consent to publish
Not applicable. The manuscript does not contain any individual person's data in any form.

Competing interests
The authors declare no competing interests.

Received: 13 November 2025 / Accepted: 12 March 2026
Published online: 26 March 2026

References

1. Kappe F, Wituschek S, Bobbert M, Meschut G. Determining the properties of multi-range semi-tubular self-piercing riveted joints. Prod Eng Res Devel. 2022;16:2–3. https://doi.org/10.1007/s11740-022-01105-2.
2. European Parliament and Council of the European Union. Regulation (EU) 2025/1214 of 17 June 2025 amending Regulation (EU) 2019/631 to include an additional flexibility as regards the calculation of manufacturers' compliance with CO2 emission performance standards for new passenger cars and new light commercial vehicles for the calendar years 2025 to 2027. [Online]. Available: http://data.europa.eu/eli/reg/2025/1214/oj
3. Friedrich HE. Leichtbau in der Fahrzeugtechnik. Wiesbaden: Springer Fachmedien Wiesbaden; 2017.
4. Li H, Liu XS, Zhang YS, Ma MT, Li GY, Senkara J. Current Research and Challenges in Innovative Technology of Joining Dissimilar Materials for Electric Vehicles, in Advanced High Strength Steel and Press Hardening, Hefei, China, Y. Zhang and M. Ma, Eds., 2019, 363–80. https://doi.org/10.1142/9789813277984_0056
5. Kasaei MM, Beygi R, Carbas RJC, Marques EAS, Da Silva LFM. A review on mechanical and metallurgical joining by plastic deformation. Discov Mech Eng. 2023;2(1). https://doi.org/10.1007/s44245-023-00012-9.
6. Meschut G, Hahn O, Janzen V, Olfermann T. Innovative joining technologies for multi-material structures, Weld World, 2014;58(1): 65–75. https://doi.org/10.1007/s40194-013-0098-3
7. Technical Bulletin DVS 3410. Self-pierce Riveting - Overview. Düsseldorf: European Research Association for Sheet Metal Working; 2019.
8. Porcaro R, Hanssen AG, Langseth M, Aalberg A. Self-piercing riveting process: An experimental and numerical investigation. J Mater Process Technol. 2006;171(1):10–20. https://doi.org/10.1016/j.jmatprotec.2005.05.048.
9. Wituschek S, Kappe F, Lechner M. Investigation of the influence of varying tumbling strategies on a tumbling self-piercing riveting process. Prod Eng Res Devel. 2022;16:2–3. https://doi.org/10.1007/s11740-021-01099-3.
10. Shao C, et al. Low-frequency vibration assisted self-pierce riveting (LV-SPR) of carbon fiber reinforced composite and aluminum alloy. Int J Mach Tools Manuf. 2024;197:104147. https://doi.org/10.1016/j.ijmachtools.2024.104147.
11. Kappe F, Bobbert M, Meschut G. Investigation of the influence of the rivet geometry on joint formation for a versatile self-piercing riveting process, Proceedings of the Institution of Mechanical Engineers, Part E: Journal of Process Mechanical Engineering, 2024, Art. no. 09544089241263141. https://doi.org/10.1177/09544089241263141
12. Kappe F. Wandlungsfähiges Halbhohlstanznieten mit linearer Prozesskinematik, Dissertation, Shaker Verlag.
13. Mori K, Kato T, Abe Y, Ravshanbek Y. CIRP Ann. 2006;55(1):283–6. https://doi.org/10.1016/S0007-8506(07)60417-X. Plastic Joining of Ultra High Strength Steel and Aluminium Alloy Sheets by Self Piercing Rivet,.
14. Yu W, Wang C, Du Z, Cheng A, He Z. Experimental and numerical investigation on the effect of process parameters on joint strength and failure behavior of self-piercing riveted steel/aluminium hybrid joints, Proceedings of the Institution of Mechanical Engineers, Part L: Journal of Materials: Design and Applications, 239(8): 1549–568, 2025, https://doi.org/10.1177/14644207241297198
15. Holtkamp P, Kappe F, Probst P, Bobbert M, Meschut G. Investigation of local heat treatment strategies for a multi-range capable rivet and the influence on joint formation and load-bearing capacity, Proceedings of the Institution of Mechanical Engineers, Part L: J Mater: Design Appl, 239(4): 787–800, 2025, https://doi.org/10.1177/14644207241307508
16. Zhang Y, Yi R, Wang P, Fu C, Cai N, Ju J. Art no 2000535. 2021;92(4). https://doi.org/10.1002/srin.202000535. steel research int.Self-Piercing Riveting of Hot Stamped Steel and Aluminum Alloy Sheets Base on Local Softening Zone,.
17. Deng L, Lou M, Li Y, Carlson BE. Thermally Assisted Self-Piercing Riveting of AA6061-T6 to Ultrahigh Strength Steel, J Manufact Sci Eng, 2019; 141(10),101006. https://doi.org/10.1115/1.4044255
18. Zhang X, He X, Xing B, Wei W, Lu J. Pre-holed self-piercing riveting of carbon fibre reinforced polymer laminates and commercially pure titanium sheets. J Mater Process Technol. 2020;279:116550. https://doi.org/10.1016/j.jmatprotec.2019.116550.
19. Wang C, Du Z, Cheng A, He Z. A comparative study on self-piercing riveting and pre-holed self-piercing riveting of high-strength steel and aluminum alloy, Proceedings of the Institution of Mechanical Engineers, Part L: Journal of Materials: Design and Applications 2025; 239(7): 1245–1265, https://doi.org/10.1177/14644207241286111

20. Böllhoff Group. NEW RIVSET® HDZ – Pioneering self-pierce riveting technology for modern material trends. [Online]. Available: https://d3pvl60m7a4hcd.cloudfront.net/asset/948671838973/document_skkj0gnt0d5ar24s30qk98nl3s/6713-RIVSET-HDZ-EN.pdf?content-disposition=inline
21. Saarstahl. Werkstoff-Datenblatt Saarstahl C35R. Accessed: Feb. 12, 2024. [Online]. Available: https://www.saarstahl.com/sag/downloads/download/9082
22. Novelis Global Automotive. Datasheet: Novelis AdvanzTM 6F - e170.
23. Voestalpine AG. Datenblatt Complexphasen-Stähle, 2024. [Online]. Available: http://www.voestalpine.com/stahl/content/download/4522/file/Datenblatt-
24. Kappe F, Zirngibl C, Schleich B, Bobbert M, Wartzack S, Meschut G. Determining the influence of different process parameters on the versatile self-piercing riveting process using numerical methods. J Manuf Process. 2022;84:1438–48. https://doi.org/10.1016/j.jmapro.2022.11.019.
25. Meschut G, Hahn O, Horstmann S, Esderts A, Sander M. Betriebsfestigkeit stanzgenieteter Bauteile: Ergebnisse eines Vorhabens der industriellen Gemeinschaftsforschung (IGF) (EFB-Forschungsbericht 429). Hannover: Europäische Forschungsgesellschaft für Blechverarbeitung e.V; 2016.
26. Self-piercing riveting. Properties, processing and applications (Woodhead publishing series in welding and other joining technologies 82). Oxford: WP Woodhead Publ; 2014.
27. Holtkamp PK. Simulation of the joining process of graded hardened multi-range capable rivets, in Material Forming: ESAFORM 2025, 2025, 1413–421. https://doi.org/10.21741/9781644903599-153
28. Hibbert DB. Experimental design in chromatography: a tutorial review, Journal of chromatography. B, Analytical technologies in the biomedical and life sciences, early access. https://doi.org/10.1016/j.jchromb.2012.01.020

Publisher's note